https://doi.org/10.5194/egusphere-2026-17
Preprint. Discussion started: 3 February 2026

UV/Vis Stratospheric Air Mass Factors considering photochemistry at two Antarctic stations

Laura Gómez-Martín[1], Cristina Prados-Roman[1], Martyn P. Chipperfield[2,3], Michel van Roozendael[4], Olga Puentedura[1], Monica Navarro-Comas[1], Hector Ochoa[5], Margarita Yela[1]

[1]Atmospheric Research and Instrumentation Branch, National Institute for Aerospace Technology (INTA), Madrid, 28850, Spain
[2]School of Earth and Environment, University of Leeds, Leeds, UK
[3]National Centre for Earth Observation, University of Leeds, Leeds, UK
[4]Royal Belgian Institute for Space Aeronomy, Brussels, Belgium
[5]National Antarctic Direction (DNA)/Argentinian Antarctic Institute (IAA), 25 de Mayo 1143, San Martín, Provincia de Buenos Aires, Argentina

Correspondence to: Laura Gomez Martin (gomezml@inta.es)

Abstract. The molecules NO_2, O_3, OClO and BrO play a major role in the photochemistry of stratospheric ozone, notably in the formation of the springtime Antarctic ozone hole. For this reason, these species have been monitored by Differential Optical Absorption Spectroscopy (DOAS) instrumentation for many decades. In order to transform DOAS Slant Column Densities (SCDs) into Vertical Column Densities (VCDs), independent of the viewing geometry, the Air Mass Factors (AMFs) relating these quantities are needed. Ground-based stratospheric trace gas measurements are performed in zenith-viewing geometry at twilight, around and beyond 90° solar zenith angle (SZA). At those solar angles, the Earth's sphericity and the rapid changes in photochemical parameters (e.g., photolysis rate coefficients) affect the calculation of the AMFs, particularly for photochemically active species such as NO_2, OClO and BrO. This study presents a methodology to infer AMFs that account for sphericity and photochemical effects. We estimate stratospheric AMFs of NO_2, O_3, OClO and BrO for Belgrano and Marambio Antarctic stations using the MYSTIC [Mayer, 2009; Emde et al., 2010] Radiative Transfer Model (RTM). The photochemical changes taking place during twilight are considered using a photochemical box-model based on the SLIMCAT chemistry transport model [Chipperfield et al., 1999, 2006]. Vertical profile concentrations obtained by this model are averaged over the optical paths and used as an input for the MYSTIC RTM. The robustness of the proposed methodology is tested against measurements of NO_2, O_3, OClO and BrO SCDs obtained at Marambio and Belgrano. A good agreement is observed between modelled and measured values of NO_2, O_3 and OClO SCDs. For BrO bigger differences are obtained but they have been attributed to the tropospheric BrO contribution that has not been included in the model. Our results show that monthly averaged AMFs can be considered as a good approximation for O_3 and BrO, but more temporally resolved sampling is recommended for NO_2 and especially OClO during July. This work shows the large impact of photochemistry for both the magnitude and also the SZA dependency of the evolution of the AMFs during twilight.

1 Introduction

Although evidence for a progressive recovery of the stratospheric ozone layer has been recently reported [WMO, 2025], the Antarctic ozone hole continues to form every year during austral spring [e.g. Solomon et al., 2014]. Therefore, long-term observations of ozone and related key stratospheric trace gases such as NO_2 [e.g. Crutzen 1979] and halogen compounds [e.g. Solomon et al., 1990; McElroy et al., 1986; Gil et al., 1992, Hendrick et al., 2007; Pinardi et al, 2022; Chong et al, 2024] remain essential. Ground-based observations performed with zenith viewing DOAS instruments [e.g., Yela et al., 2017, Yela et al., 2005] have allowed the accumulation of multi-decadal time-series of O_3, NO_2, BrO and OClO columns. OClO is formed from the reaction between BrO and ClO and can provide a good proxy for chlorine activation [Sander and Frields, 1989]. Using the DOAS retrieval technique, differential Slant Column Densities (dSCDs) of gases absorbing in this UV-visible spectral region can be obtained (dSCD = SCD + SCDref where SCDref refers to the chosen reference spectrum). SCDs represent the concentration of a given molecule integrated over the optical path of the sunlight through the atmosphere to the instrument. INTA has been operating UV-VIS DOAS spectrometers at the Belgrano (77ºS) and Marambio (65ºS) Antarctic stations since 1994 [Yela et al., 2017]. Since 2016, both stations are part of the Network for the Detection of Atmospheric Composition Change (NDACC, www.ndacc.org), that aims to monitor the evolution of the atmospheric composition, evaluate the impact of the observed changes, provide valuable data for satellite validation, fill in satellite data gaps and test atmospheric models. Currently, this network is composed of more than 70 stations and 160 ground-based remote sensing instruments.

During twilight, SCDs provide information on stratospheric trace gases. However, SCDs are dependent on the viewing geometry. Thus, to compare measurements performed at different times or places, SCDs are usually transformed into corresponding Vertical Columns Densities (VCDs), which only depend on the atmosphere and the geometry of the sun. The variable relating both quantities is the Air Mass Factor (AMF = SCD/VCD by definition). AMFs are computed using Radiative Transfer Models (RTM), which require an a-priori knowledge of the state of the atmosphere, i.e. vertical profiles of the different gases, temperature, pressure, etc. Since 2012, the ground-based DOAS community working on stratospheric research [e.g. Adams et al., 2012], has used O_3 and NO_2 AMFs provided by NDACC [Hendrick et al., 2011]. These NDACC AMFs are provided monthly in latitude bins of 10° between 85ºS and 85ºN and consider surface albedo equal to 0 and 1 and SZAs extending from 30° to 92° (for NO_2, AMF for 10º is also included). NDACC O_3 AMFs are computed from 440 nm to 580 nm in steps of 35 nm, and for NO_2 from 350 nm to 550 in steps of 40 nm, using the pseudo-spherical DISORT RTM [Kylling and Mayer, 2003]. Input profiles are based on the Total Ozone Mapping Spectrometer (TOMS) v8.0 [Barthia et al., 2004] climatology for O_3 and on the Lambert et al. [1999, 2000] climatology supplemented by SAOZ balloon soundings for NO_2. NDACC O_3 AMFs take into account the whole atmosphere from the surface up to the stratosphere, while for NO_2 the AMFs are exclusively stratospheric (from 12 km upward). Twilight photochemistry is neglected in NDACC AMFs.

With regard to BrO, there is little literature on stratospheric AMFs. In the recent work of Chong et al. [2024], BrO AMFs have been calculated with the *Vector LInearized Discrete Ordinate Radiative Transfer Model* (VLIDORT, [Spurr, 2006, 2008; Spurr and Christi, 2019]) using input from the *Community Atmosphere Model with Chemistry* (CAM-Chem) climatology [Fernandez et al., 2019], to analyse a decade of data obtained by the Ozone Mapping and Profiling Suite Nadir Mapper (OMPS-NM) onboard the Suomi National Polar-orbiting Partnership (Suomi-NPP) satellite [Flynn et al., 2014]. In the work of [Theys et al., 2007], [Hendrick et al., 2007] and [Koenig et al., 2024], BrO AMFs are used to analyse ground-based DOAS measurements from Reunion Island (21ºS), Harestua (60ºN) and Mauna Loa (19ºN) stations, respectively. In [Theys et al., 2007] and [Hendrick et al., 2007], the setup applied for the BrO retrieval includes the DISORT pseudo-spherical RTM coupled with the SLIMCAT 3-D chemical transport model (CTM) and the stacked-box photochemical model PSCBOX [Errera and Fonteyn, 2001; Hendrick et al., 2004]. A similar setup is used in [Koenig et al., 2024] but based on the CAM-Chem model [Lamarque et al, 2012] profiles. Regarding OClO, stratospheric AMFs are calculated in Pukite et al. [2022] using the 3-D full spherical RTM McArtim [Deutschmann et al., 2011; Deutschmann, 2014] to analyse data from the *TROPOspheric Monitoring Insrument* (TROPOMI) onboard the Copernicus Sentinel-5 Precursor platform. In all of these studies, the AMF calculations are mostly limited to SZAs <= 90° and AMFs values are not explicitly provided. To our knowledge, the only publication showing OClO AMFs for SZA up to 95º is Pinardi et al. [2023]. In that work, ground-based DOAS instruments at 9 NDACC stations covering polar regions from both hemispheres are used to validate OClO measurements by the GOME-2 satellite instrument. Ground-based OClO values are offset corrected using a Langley plots approach making use of empirically-derived OClO AMFs. Finally, in Kühl et al. [2004], OClO AMFs are estimated with the AMFTRAN radiative transfer model [Marquard et al., 2000] for different Gaussian vertical profiles and for SZAs between 40º and 95º. However, the specific OClO concentration profiles are not shown.

In the present work, the stratospheric AMFs of NO_2, O_3, OClO and BrO are estimated using the Monte-Carlo MYSTIC Radiative Transfer Model (RTM) [Mayer, 2009; Emde et al., 2010] for Marambio and Belgrano stations (Section 2.3), for SZAs up to 94º. Photochemistry taking place during twilight is considered using a photochemical box-model based on the SLIMCAT 3-D CTM (Section 2.1, [Denis et al., 2005; Chipperfield, 2006]). Optical path averages of the concentration profiles are calculated following the method described in Section 2.2. Section 3 introduces the ground-based observations used to validate our approach. The observed AMF results are shown and compared with previous work and ground-based observations in Section 4. Our main conclusions are summarised in Section 5.

2 AMF Calculation Method

The AMFs presented in this work are calculated in the UV and in the Vis spectral range: at 510 nm for O_3, 470 nm for NO_2, 351 nm for OClO and 355 nm for BrO at Marambio and Belgrano stations. The wavelengths used for O_3 and NO_2 correspond to those routinely applied in Marambio and Belgrano for NDACC retrievals. The wavelengths selected for BrO and OClO are chosen for being close to the maximum absorption of those species in the spectral range used in our DOAS measurements (see Section 3). We follow a four-step approach as depicted in Fig. 1:

1. In a first step, a photochemical 1-D stacked box-model coupled to SLIMCAT [Chipperfield, 1999, 2006] is run with a 5-minute timestep to obtain the daily SZA-dependent vertical profiles (288 SZAs per day) of O_3, OClO, BrO, NO_2, H_2O, pressure (P) and temperature (T) for Marambio and for Belgrano for a whole year. These are grouped as monthly (sunrise-am and sunset-pm) averaged profiles for SZAs from 80º to 94º in steps of 1º. The values of the SZAs at each station depend on the time of the year considered. Whenever possible, AMFs for SZA= 50º, 60º and 70º are also calculated. The motivation of grouping the profiles monthly is to reduce data processing. The validity of using monthly averages versus 10-day-averaged values is evaluated in Section 2.2.2.
2. In a second step, the concentration profiles obtained with the box model are averaged over the SZAs encountered along the optical path for each atmospheric layer (c_l), taking into account the spherical geometry. This is described fully in Section 2.2.
3. Then, by using those averaged profiles as input, Box-AMFs (a_l) and SCDs are computed using the MYSTIC RTM [Mayer, 2009; Emde et al., 2010].
4. Finally, total AMFs are calculated as explained in the following paragraph.

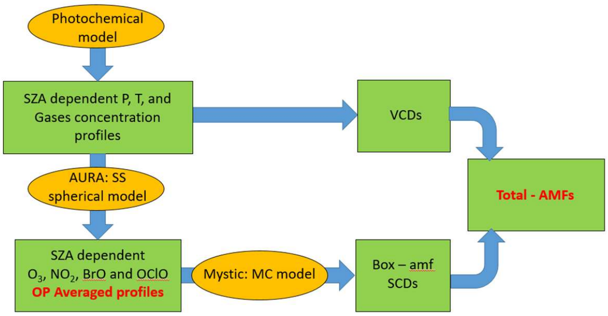

Figure 1: Summary of the AMF retrieval method.

Box-AMFs (a_l) relate the optical path followed by sunlight at each atmospheric layer (ds_l) with the vertical layer thickness (dz_l):

$$a_l = \frac{ds_l}{dz_l}, \qquad (1)$$

In this work, atmospheric layers of 1 km thickness have been considered from the surface to an altitude corresponding to 0.13 hPa (55-62 km, depending on the time of the year), treated here as the top of the atmosphere (TOA). From the vertical profiles

https://doi.org/10.5194/egusphere-2026-17
Preprint. Discussion started: 3 February 2026

of the considered gases and these Box-AMFs, the total VCDs, SCDs and the corresponding AMFs can be calculated by integrating concentration over the optical path (slant or vertical) from the surface to the TOA:

$$vcd_l = c_l dz_l \,, \tag{2}$$

$$VCD_{total} = \sum_0^{TOA} vcd_l \,, \tag{3}$$

$$scd_l = vcd_l a_l dz_l \,, \tag{4}$$

$$SCD_{total} = \sum_0^{TOA} scd_l \,, \tag{5}$$

$$AMF_{total} = \frac{SCD_{total}}{VCD_{total\_ph}} \,, \tag{6}$$

where c_l is the average concentration of the considered trace gas in each layer l, vcd_l and scd_l are the partial VCD and SCD in each layer, and SCD_{total}, VCD_{total} and AMF_{total} are total SCD, VCD and AMF values. Note that in all these equations, vcd_l are calculated using the averaged concentrations, but for AMF_{total}, we use the VCD_{total_ph} (eq. 6) calculated from the vertical profiles obtained with the 1-D photochemical model.

Figure 2 presents some examples of these Box-AMFs for Marambio with a surface albedo = 0 in the UV and in the Vis. Note that, as expected for the higher SZA values, Box-AMFs below 10 km are small, due to the limited contribution of the troposphere to the optical path for this high SZA. Figure 2 shows that Box-AMFs peak at higher altitude at UV than at visible wavelengths, and the maxima of these peaks are also higher. Due to the lower attenuation of visible radiation, visible Box-AMFs extend to lower altitudes.

https://doi.org/10.5194/egusphere-2026-17
Preprint. Discussion started: 3 February 2026

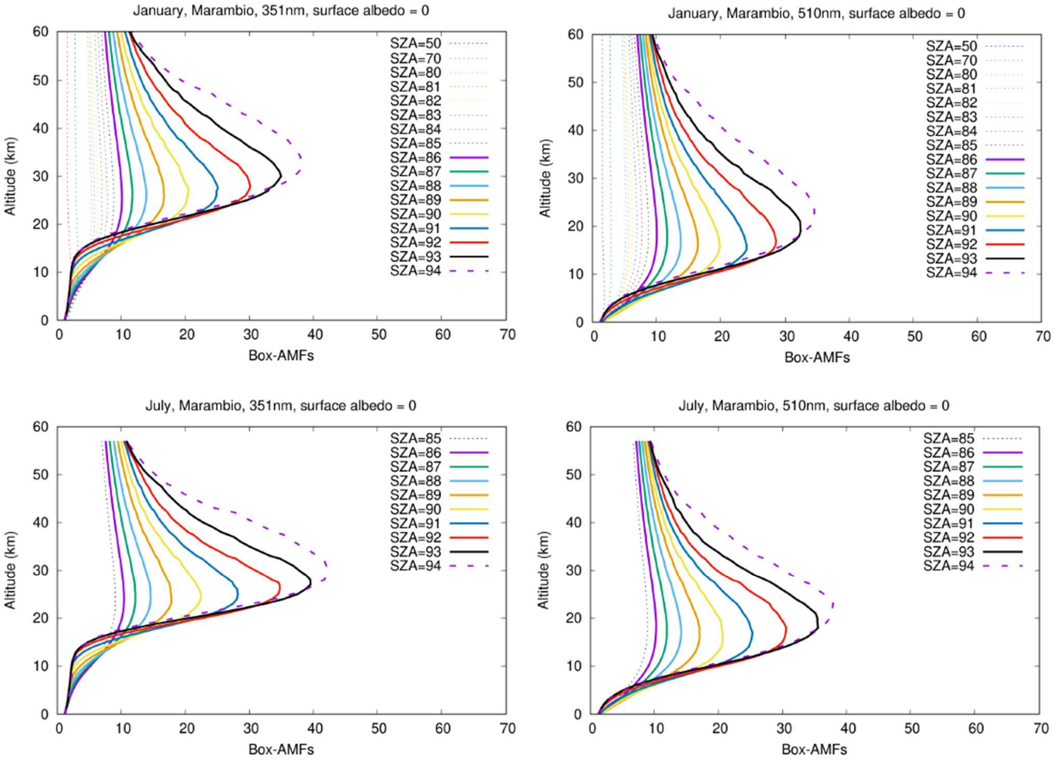

Figure 2: Box-AMFs computed for Marambio, corresponding to January (top) and July (bottom) 2018, for surface albedo=0 and different SZAs (see legend). Left panels are Box-AMFs in the UV (351 nm), right panels are Box-AMFs in the Vis (510 nm).

2.1 TOMCAT/SLIMCAT model simulations

Our analysis uses results from the TOMCAT/SLIMCAT (hereafter SLIMCAT) 3-D CTM [Chipperfield 1999, 2006]. First the full 3-D model is used to perform a long-term simulation (see e.g. Dhomse et al. [2022]). The model was run from 1979 to 2024 at a horizontal resolution of 2.8º × 2.8º and 32 levels from the surface to around 60 km. This simulation was forced using meteorology from ECMWF ERA5 renalyses [Hersbach et al., 2020]. The model has a detailed stratospheric chemistry scheme including long-lived source gases, such as CH_4, N_2O, halocarbons, and the chemical families Ox, NOy, HOx, Cly and Bry. It also includes selected brominated and chlorinated very short-lived substances (VSLS), including $CHBr_3$ and CH_2Br_2. The chemistry is constrained by specified time-dependent monthly global mean surface mixing ratios of the long-lived tracers [WMO, 2022]. The two brominated VSLS both have constant tropospheric mixing ratios of 1 pptv, which together contribute a total 5 pptv to stratospheric bromine. Photochemical data used in the model is taken from NASA/JPL (2019). In addition to gas-phase chemistry, the model includes a detailed treatment of heterogeneous chemistry on liquid sulfuric acid aerosols along with liquid and solid polar stratospheric clouds (PSCs).

Daily (00 UTC) outputs from the full 3-D simulation are stored for the locations of Marambio and Belgrano. This is then used as an input for daily simulations of a 1-D (column) chemical model based on the same SLIMCAT chemical scheme without transport. The goal of this 1-D chemical model is to obtain the photochemical state of the atmosphere (i.e., concentrations of the different target gases) at much high temporal resolution than could be obtained directly from the 3-D model. The 1-D model is integrated each day with a 5-minute timestep and the fields of the target gases are saved for each timestep, providing a dataset of concentrations at varying SZA for every day.

2.2 Accounting for photochemistry along the light path

The concentration profiles provided by the photochemical model are representative for a horizontal resolution of 2.8º (the horizontal resolution of the SLIMCAT 3D-CTM). However, for large optical paths, the angle at which the solar beams reach each atmospheric layer (far away from the station) can be very different from the SZA over the station (Fig. 3), and thus the gas concentration can also differ substantially. The larger the SZA over the station, the greater the difference in the angle that each incident solar beam forms with each layer. Thus, the concentration of a given gas in a given atmospheric layer encountered by the sunlight reaching an instrument at the surface, for SZA = θ ($c_{l,\theta}$), is actually an average of the concentrations corresponding to all values of the SZAs encountered by all the beams passing through this layer along their optical paths (see Fig. 3). To take this effect into account, we average the concentrations of the target species over the optical path using a ray-tracing model, AURA, developed for this purpose at INTA. There are two reasons to proceed in this way: (1) the multi-scattering Monte Carlo (MC) MYSTIC model used in this work is a 1-D model, which means that only one profile for each target species can be introduced in the model for the whole atmosphere. Thus, we want to use a concentration profile representative of the whole atmosphere that takes chemistry into account. (2) By doing this, we validate a method that simplifies calculations and that can be used for other studies. To average the concentrations along the light path, we make some approximations. First, we assume that solar rays are scattered only once before reaching the surface, and we divide the atmosphere into layers 1-km thick, with the top of the atmosphere (TOA) at 65 km. Note that, for an absorber above 15 km altitude and wavelengths between 350 and 650 nm, the single scattering is already a good approximation for zenith-sky stratospheric AMFs [Perliski and Solomon, 1993]. Figure 3 illustrates the geometry of the problem; panel (a) shows the optical path followed by the solar beams before reaching the surface for SZAs up to 90º at the vertical of the station; panel (b) shows the same information for SZAs > 90º. In the first case, solar beams pass through each layer just once. In the second case, a solar beam can pass through a given layer once or twice slantwise and once vertically (see Figure 3 b and c)). In these figures, we have labelled the SZA at which a solar beam crosses a layer as θ_1 (bottom of the layer) and θ_2 (top of the layer). Analogously, when the solar beam passes through the layer a second time, θ_3 and θ_4 are the SZAs at which the solar beam reaches the bottom and the top of the layer. Note that, when the scattering is produced above the layer considered, this layer is crossed vertically and the concentration at SZA = θ is then considered. For each SZA and each layer the partial slant column, scd_l , can be calculated as follows:

$$scd_l = \sum_b \frac{I_b}{I_{tot}} \left(\sum_i c_{b,l,i} s_{b,l,i} \right), \tag{7}$$

where subscript b is for each solar beam, l is for each layer, and i is for all the partial optical paths, $s_{b,l,i}$, and the corresponding concentrations, $c_{b,l,i}$, that each beam sweeps through the same layer (red lines in Fig. 3). I_b is the contribution of each beam to the total intensity, I_{tot}, measured at surface [Solomon et al., 1987]. To simplify this we can consider a concentration, c_b', equivalent to all the concentrations that a given beam experiences when crossing successive layers:

$$\sum_i c_{b,l,i} s_{b,l,i} = c'_{b,l} \sum_i s_{b,l,i} = c'_{b,l} S_{b,l}, \tag{8}$$

$$c'_{b,l} = \sum_i \frac{s_{b,l,i}}{S_{b,l}} c_{b,l,i}, \tag{9}$$

Introducing (9) in (7):

$$scd_l = \sum_b \frac{I_b}{I_{tot}} c'_{b,l} S_{b,l}, \tag{10}$$

Analogously, we now calculate the final averaged concentration for each layer, $c_{ave,l}$, as follows:

$$\sum_b \frac{I_b}{I_{tot}} c'_{b,l} S_{b,l} = c_{ave,l} S_l, \tag{11}$$

$$c_{ave,l} = \sum_b \frac{I_b}{I_{tot}} \frac{S_{b,l}}{S_l} c'_{b,l}, \tag{12}$$

If we now introduce (12) into (10), we have:

$$scd_l = c_{ave,l} S_l, \tag{13}$$

By doing this, we now have an averaged concentration for each SZA and each layer that represents all the concentrations found by all beams that pass through this layer.

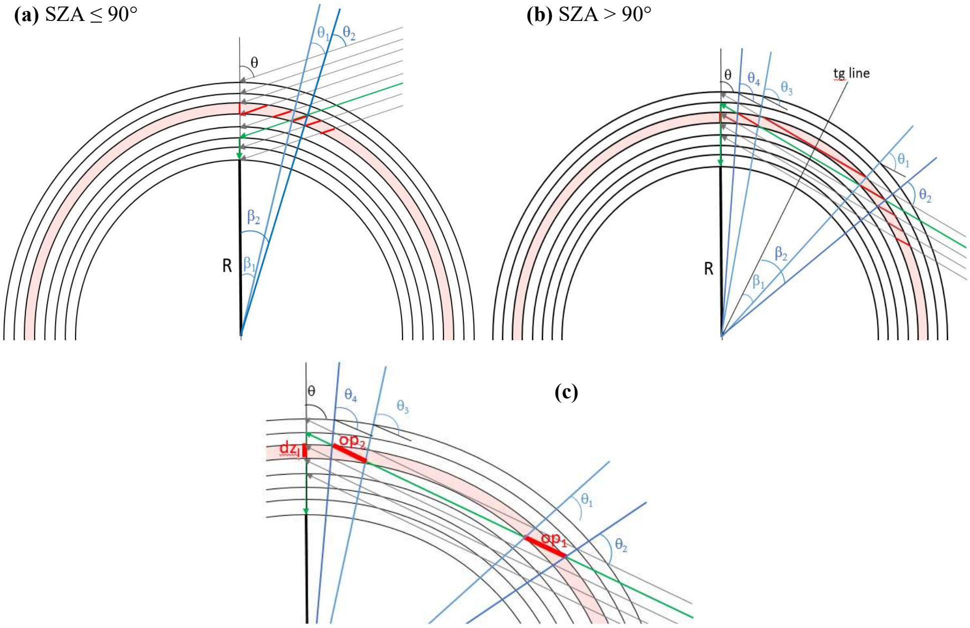

Figure 3: Schematic showing how spherical geometry is taken into account in the calculation of the averaged trace gas concentrations. Panel (a) shows the case for SZA≤90 ° is shown. Panel (b) represents the case for SZA>90º. In panel (c) the partial optical paths for one beam and one layer are shown.

In some cases, the solar beam does not touch the bottom of the layer, for example see lower solar beam (grey arrows) in Figure 3b, and the lower layer. In that case, the mean concentration is calculated between the concentration at the top of the layer and at the minimum altitude reached by the beam at that layer.

As has been indicated in the equations, the contribution of each beam to the SCD is weighted by its contribution to the total intensity observed at the surface, I_b/I_{tot}, [Solomon et al., 1987]. In Figure 4, the contribution of the intensity observed at the surface by an instrument looking at zenith as a function of the scattering altitude is represented for different SZAs, (the scattering altitude being the vertical distance from the instrument at which sunlight beams are scattered towards the instrument). Due to the lower attenuation (optical depth) at visible wavelengths, the scattered intensity at the surface is higher in the visible than in the UV. Also, UV solar beams are scattered towards the surface at higher altitudes compared to visible ones, since more UV radiation is available above the station at those altitudes.

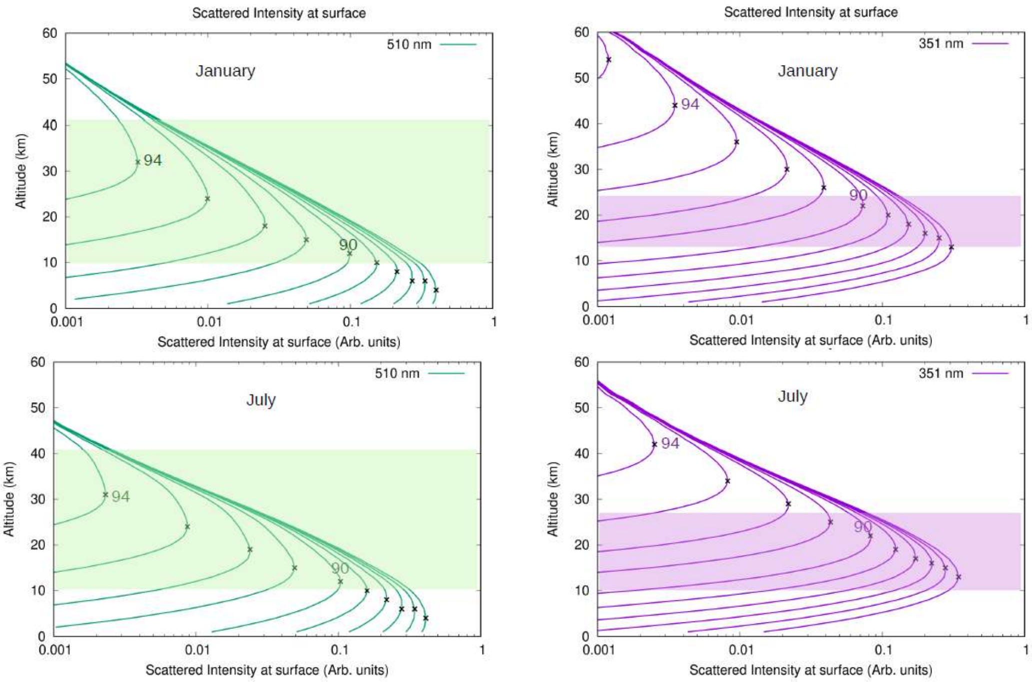

Figure 4: Scattered intensity reaching the surface for a zenith-looking instrument, as a function of the scattering altitude. Green lines (left) are the corresponding curves for the visible (510 nm) spectral range, and violet lines (right) correspond to the UV (351 nm) spectral range. Values for SZA from 85º to 94º (510nm) and to 95º (351 nm) in steps of 1º are represented. The corresponding maxima of each of these curves (maximum scattering altitude) are represented by black crosses. Shadowed regions correspond to the altitudes where most of the O_3 or NO_2 (green) and BrO or OClO (violet) are found (from chemical model profiles used in this work). Calculations are performed for January (top panels) and July (bottom panels) 2018 at Marambio.

Figure 5 shows some examples of how the concentration profiles change after averaging their values as described above. For species such as O_3, or for low SZA for which solar beam optical paths stay close to the station, the concentration profiles do not change appreciably after averaging. However, for photochemically active species such NO_2, BrO or OClO, this can have a big impact on the profiles, especially for high SZAs. The impact of considering these averages in the final results is discussed in Section 3.

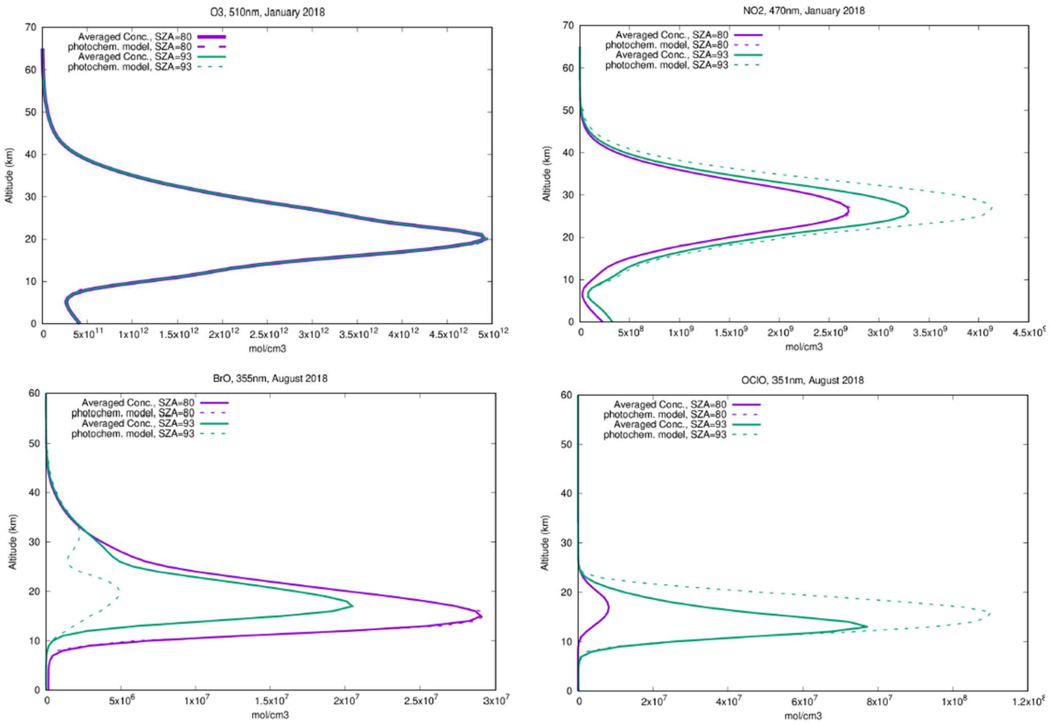

Figure 5: Comparison of vertical concentration profiles for Marambio as they are output by the 1-D chemical model above the station (dashed lines) and after averaging (solid lines) over the optical path as described in the text. Profiles for SZA=80º (above the station) are represented in violet, and for SZA=93º in green. Top left: O_3 profiles calculated at 510 nm for January; Top right: NO_2 profiles calculated at 470 nm for January; Bottom left: BrO profiles calculated at 355 nm for August; Bottom right: OClO profiles calculated at 351 nm for August.

To check the validity of these approximations, SCDs of the four target species obtained using AURA in 2-D mode and considering the photochemical model concentration profiles (different for each SZA), have been compared with the SCDs obtained with AURA in 1-D mode, using a single averaged concentration profile (eq. 12) for the whole atmosphere. Results are almost identical (See Figures S1 – S4 of the Supplementary Material), meaning that the calculated averaged profiles reproduce well SCDs obtained from the SZA-dependent profiles. In addition, SCDs obtained with AURA have been compared with a ray tracing model developed at BIRA that has been validated against other codes [Hendrick et al., 2006], showing in general similar results as AURA (See Figures S1 – S2 of the Supplementary Material).

2.3 MYSTIC radiative transfer simulations

MYSTIC [Mayer, 2009; Emde et al., 2010] is a fully spherical Monte Carlo (MC) radiative transfer code. Simulations performed with this code have been compared to different benchmark results [Emde et al., 2010] and other RTMs [Zawada et al., 2021] showing consistently good agreement. In MYSTIC, individual photons are traced on their random paths through the atmosphere in order to obtain solar-radiation-related magnitudes as radiances, irradiances, actinic fluxes, optical paths and Box-AMFs, for given viewing and solar geometries. Even though MYSTIC was originally conceived as a 3-D model to consider complex cloud shape [Mayer, 2009] and/or topography [Mayer et al., 2010; Schwaerzd et al., 2021], for the purpose of this work the standard Box-AMF output of 1D-MYSTIC provided in version 2.0.4 of libRadtran software package [Emde et al., 2016; Mayer and Kylling, 2005] have been used, since it is the only version available in libradtran and clouds or complex surface topography are out of the scope of this work. An assessment of cloud effect can be found in e.g. Pukite et al. (2022). By using this fully spherical code: (1) we use the real geometry; (2) we test a RTM that is freely available for the community; and (3) we are able to assess how fully spherical simulations compare with pseudo-spherical ones (see Section 4.1).

2.3.1 RTM settings

As explained above, O_3, OClO, BrO, NO_2, H_2O, P and T vertical profiles in our calculations are taken from the 1-D photochemical box-model and averaged along the light path as explained in Section 2.2. Except in very rare cases when aerosols reach the stratosphere (i.e. volcanic or fire ashes), aerosols have a low influence. Thus, no aerosols are considered in our calculations. Sensitivity tests have been performed (not shown here) introducing aerosol with AOD=0.1, exponentially decreasing profile with a scale height = 1 km, asymmetry parameter = 0.6, and single scattering albedo = 0.9. Differences in Box-AMFs with and without aerosols are less than 1%. The solar spectrum of Kurucz [1992] is set as the solar source in our simulations. Two extreme cases of surface albedo (SA) are considered: SA=0 and SA=1. AMFs for intermediate values of SA can be estimated by interpolating between these two.

An important parameter to take into account in the MC RTM is the number of photons used in the simulations. To avoid statistical instabilities in our results, we performed several calculations changing the number of photons for the different SZAs (see Fig. 6). The higher the SZA, the lower the probability of a photon reaching the ground-based instrument. Thus, the number of photons that need to be considered increases with the SZA. In our calculations, we have set the number of photons to 10^6 for SZAs between 50º and 90º, 10^7 for SZAs between 91º and 93º, and 5×10^7 for SZA = 94º. By using these numbers we observe a smooth profile of the Box-AMFs in all cases (Fig. 6).

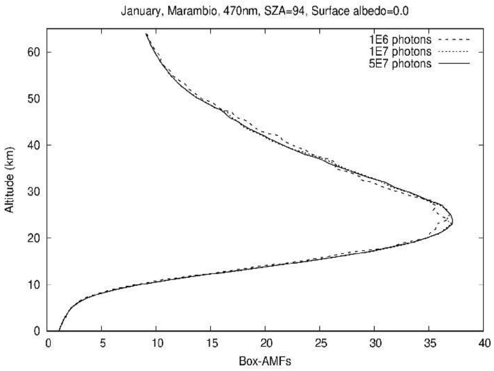

Figure 6: Box-AMFs computed for Marambio, January 2018, for SZA=94º, surface albedo=0, a wavelength of 470nm and different number of photons: 1×10^6 (dashed line), 1×10^7 (dotted line), 5×10^7 (solid line).

2.3.2 Temporal sampling of the AMFs

In order to evaluate if the use of monthly averaged AMFs is a good approximation, we have compared monthly averaged AMFs with 10-day averaged AMFs for O_3, OClO, BrO and NO_2 and for SA = 0. Note that an even shorter period of time could have been chosen, daily averages for instance, however, to perform these calculations for 2 stations, 4 spectral ranges, 2 surface albedos and 36 time periods (10-days intervals in a year) means that the number of calculations is $2 \times 4 \times 2 \times 36 = 576$ calculations with AURA and 576 with MYSTIC. Performing daily averages would mean that $2 \times 4 \times 2 \times 365 = 5840$ calculations should be performed with AURA and then with MYSTIC, which is prohibitive. In addition, by performing 10-day averages, outlier values, not representative of the "normal" variability, are smoothed. Figure7 (left) shows results for Marambio where, compared to Belgrano, a higher number of twilights (SZAs from 90º to 95º) are available. In the right panel of Figure 7, relative differences between 10-day averages and interpolated monthly values for SZA=92º are shown. Similar results are obtained for SZA= 93º and 94º, and for SA = 1. The figure shows that O_3 relative differences are always under 2%. Thus, since AMFs follow a smooth temporal variability, using monthly values can be considered as a good approximation. Maximum relative differences for BrO are below 7% most of the year, except during summer where these differences increase up to 14%. We conclude that monthly values are still a reasonable approximation. Also, for NO_2, relative differences are below 8% except during the month of June (minimum in NO_2) when the differences reach 19%. In contrast, OClO shows a high temporal variability during the chlorine activation period. Thus, if the goal of using the AMFs is to reveal annual or inter-annual variability, the use of monthly averages is justified. However, for the study of specific episodes (a few days), daily or even more resolved sampling is recommended for OClO.

https://doi.org/10.5194/egusphere-2026-17
Preprint. Discussion started: 3 February 2026

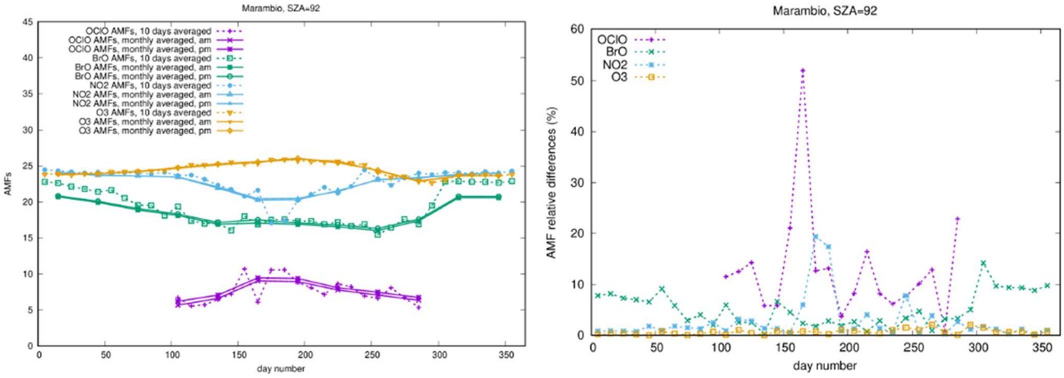

Figure 7: Left panel: OClO (violet), BrO (green), NO_2 (blue) and O_3 (yellow) stratospheric AMFs computed for Marambio, for SZA=92º, and surface albedo=0. Continuous lines correspond to monthly averaged values; dashed lines correspond to 10-day averaged values. Right panel: Relative difference between monthly and 10-day averaged AMFs: OClO (violet), BrO (green), NO_2 (blue) and O_3 (yellow). Note that for OClO only the period in which it is observed is shown in the figure.

3 Ground-based DOAS observations

The measurements used for the validation of our AMF calculation approach rely on ground-based MAX-DOAS instruments [Platt and Stutz, 2008] operated at the Antarctic stations of Marambio (64º 13’ S, 56º 37’ W) and Belgrano II (77º 52’ S, 34º 7’ W). At each of these sites, INTA has deployed MAX-DOAS systems operating in the visible and UV spectral ranges (for O_3/NO_2 and BrO/OClO, respectively). At SZA<85º, these instruments perform vertical scans of the atmosphere with small telescopes moving from the horizon to the zenith, capturing scattered skylight. During morning and evening twilights, the telescopes are fixed in zenith-viewing geometry to focus on the measurement of stratospheric gases such O_3, NO_2, BrO and OClO. Details on the design of the instruments can be found in Prados-Roman et al. [2018] and Gomez-Martin et al. [2021]. Spectral radiance data are analysed using INTA’s analysis software LANA [Gil et al., 2008; Peters et al., 2017]. NO_2 is processed in the spectral range 425-490 nm [Kreher et al., 2020]), O_3 in 450-534 nm [Hendrick et al, 2011], BrO in 346-359 nm [Alliwel et al., 2002] with updated cross-sections [O3: Serdyuchenko et al, 2014; O4: Finkenzeller and Volkamer, 2002, OClO: Kromminga et al, 2003], OClO in 345-389 nm [Pinardi et al., 2022]. Measurements used in this work refer to observations performed in 2018.

4 Results

4.1 AMF calculations for O_3, NO_2, BrO and OClO

Applying the method described in Section 2, stratospheric AMFs were calculated for the four target species O_3, NO_2, OClO and BrO. Results for surface albedo = 0 are shown in Figure 8 for Marambio and Figure 9 for Belgrano. Differences between AMFs calculated for albedo = 0 and albedo = 1 are very small (i.e., for 90°SZA, less than 0.8% for O_3 and NO_2, up to 2% for BrO and 3% for OClO for September). The values of the AMFs calculated in this work are provided in the Supplementary Material. The validity of our calculations in the Vis spectral range is tested by comparing our O_3 and NO_2 AMFs with those from NDACC which have been used since 2012 as a reference for the DOAS scientific community. The validity of our UV results is evaluated by comparing them with data available from the literature. For SZAs up to 93º, our results are also compared to AMFs obtained with the pseudo-spherical 2D-DISORT [Hendrick et al., 2004]. This comparison, which addresses both UV and visible AMFs, is restricted to albedo = 0, since large differences are not observed in the AMFs for other albedo values. In Figure 8, for O_3 and NO_2 our results have been cross-checked with the February and September O_3 and NO_2 AMFs used for NDACC (red dot symbols in the figures), for the same surface albedos and wavelengths and for a latitude of 65ºS (close to the latitude of Marambio) [Hendrick et al., 2011]. In Figure 9, our O_3 and NO_2 results for Belgrano have been also cross-checked with the February and September O_3 and NO_2 AMFs used for NDACC (red dot symbols), for the same surface albedos and wavelengths, and for a latitude of 75ºS (close to the latitude of Belgrano). In the same figures, 2D-DISORT AMFs for the same example months (February: violet dots; September: black dots) are also shown. As SZA=90º is the value used to report VCDs within NDACC, we discuss results using the AMF values at this SZA as reference. For O_3 at Marambio, our results are similar to NDACC as well as 2D-DISORT values, showing maximum relative differences of 1.8% (NDACC) and 0.6% (2D-DISORT) larger AMFs for September with even smaller differences for February. However, these differences increase up to +26% when comparing NO_2 AMFs from this study with NDACC data, while the difference with 2D-DISORT simulations remains low (1.2%). Regarding Belgrano, our results for O_3 show differences with NDACC always below 3.5% and the same with 2D-DISORT values. For NO_2 these differences increase with SZA up to 29.0% for NDACC and remain below 1.0% for 2D-DISORT. To better understand the origin of these deviations, we consider the differences between the methods used to obtain these different data sets. First pseudo-spherical RTM have been used for NDACC and 2D-DISORT AMFs in contrast with the fully spherical RTM used in this work. However, given that DISORT and MYSTIC are providing similar results (see Figures 8 and 9 and S3.1), this geometrical difference cannot explain the observed differences. Concerning vertical profiles, NDACC AMFs use the TOMS v8.0 [Barthia et al., 2004] climatology for O_3, and Lambert et al. (1999, 2000) climatology in combination with SAOZ balloon soundings for NO_2 as vertical profiles of these molecules, provided for latitudes from 85ºS to 85ºN in steps of 10º. Twilight photochemistry and optical path averages taken into account in this work are not considered in the NDACC AMF calculation. In the case of 2D-DISORT and MYSTIC, outputs of the photochemical model described in Section 2.1, specific for 2018, considering a region of 2.8º around the station, are used directly (DISORT) or averaged to obtain equivalent concentration profiles that take into account photochemistry (MYSTIC). That means that the geographical region considered in this work is significantly smaller than the latitude belt (10º) considered for NDACC. In addition, the concentration profiles used in this work are specific for the year 2018, while NDACC AMFs use climatological data published 25 years ago. Thus, what seems to be the most probable factor causing the observed differences is the different concentration

https://doi.org/10.5194/egusphere-2026-17
Preprint. Discussion started: 3 February 2026

profiles considered in each set of data. For species like O_3, whose composition and distribution with altitude do not suffer large variation during twilights, these differences do not have a big impact on the results as can be seen in Figure 8. For other species with larger variations in their vertical profiles during twilight (e.g., NO_2), the differences in AMFs are more important. This fact is of special relevance for the short-lived molecules BrO or OClO. In this case, there are very few AMF values available in the literature for comparison. In Figures 8 and 9, we compare our results with those of Pinardi et al., (2022) for OClO, and Theys et al., (2007) for BrO. Note that for BrO, we have not found any published reference of the AMFs for SZA higher than 90º. In both cases, we have also compared MYSTIC with 2D-DISORT calculations. In the work of Pinardi et al. (2022), AMFs are obtained as the ratio between SCDs for different SZAs and the VCD at SZA=70º. To properly compare our results with those of Pinardi et al. (2022), AMFs referred to VCD=70º for September have also been included in Figure 8 as blue dots. Differences in both sets of data are of 7% for sunrise and 18% for sunset (both at SZA=90º). In contrast to other species, for which AMFs increase with SZA, the stratospheric OClO AMFs obtained in this work show a local minimum close to SZA=93º for most of the year, also observed in [Kühl et al, 2004]. This results from the strong increase of the OClO concentrations beyond 90° SZA. Comparisons with 2D-DISORT simulations show absolute differences lower than 0.5 for Marambio, and 0.3 for Belgrano. For BrO, both 2D-DISORT and MYSTIC present an important increase of the AMFs with SZA, due in this case to the strong decrease of the BrO concentration beyond 90° SZA. Note that in the visible spectral range, the maximum scattering altitude ranges between 12 and 42 km for SZA between 90º and 95º (see Fig. 4). This coincides with the bulk altitude of both O_3 and NO_2 concentrations (see Figs. 4 and 5). In the UV spectral range, the maximum scattering altitude ranges between 22 to 54 km for SZA (see Fig. 4), while the bulk of the OClO and BrO concentrations is located between 10 and 25 km (see Figs. 4 and 5), i.e., mostly below the scattering altitude. However, while OClO increases at low sun and essentially remains in the same altitude range, BrO decreases and its maximum concentration moves towards higher altitudes, where the main scattering takes place (see Fig. 10). This fact was already observed in the work of [Perliski and Solomon, 1993]. There is also another factor contributing to these different behaviours between the different species AMFs. When photochemistry is not considered, the only factor changing with the SZA is the optical path that increases with the SZA. However, when photochemistry is considered, not only does the optical path change but also the vertical profile of the species. As the AMFs is the ratio between the SCD and the VCD, the value of the AMFs depends on the evolutions of the VCD and SCD , which are affected not only by the optical path but also by the changing profile concentration. Note that, when calculating the optical path SCD average, we consider the concentration vertical profiles observed across the optical path, with SZA increasing up to the SZA above the station (see Fig. 4). These paths experienced lower SZA, corresponding to lower concentrations of NO_2 and OClO but higher concentrations of BrO (see Fig. 5). Thus, when the SZA increases, the SCD averaged over the optical path is lower than the SCD calculated for the SZA over the station for NO_2 and OClO and higher for BrO. As already noted, this also contributes to the evolution observed in the twilight AMFs of these molecules.

All of the features explained above are also applicable to the Belgrano station (see Fig. 9). In this case, the number of months for which the sunlight reaches our instrument is smaller than for Marambio, thus the number of AMFs is also smaller. However, the behaviour of the AMFs calculated for all of the molecules is similar to that observed at Marambio.

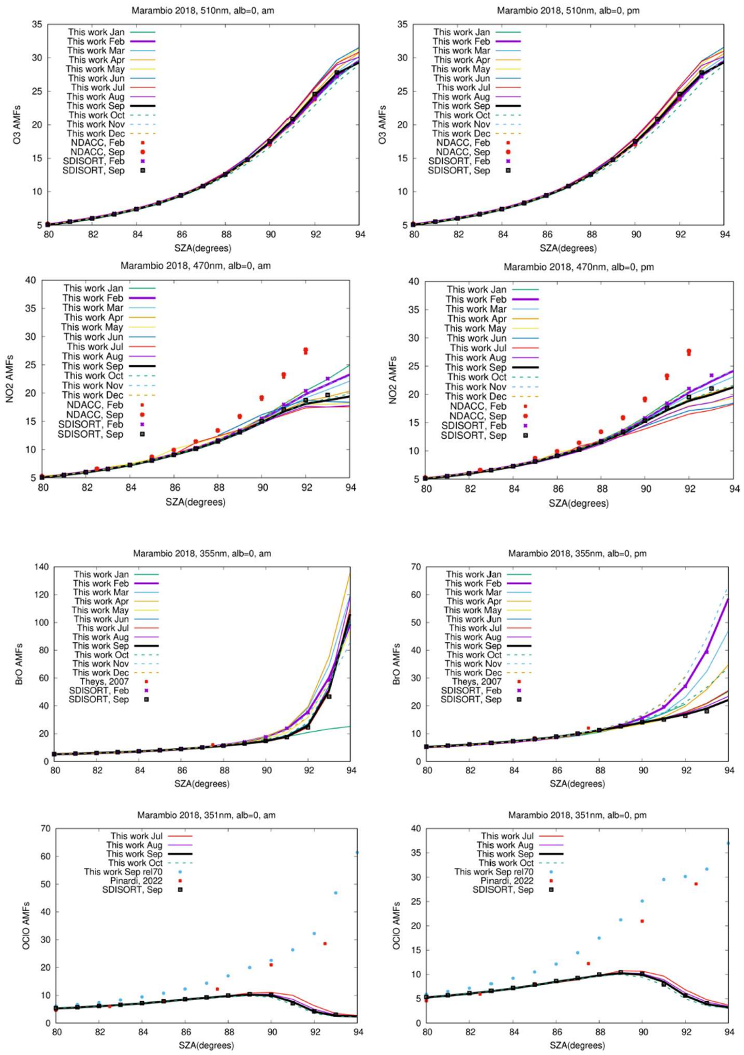

Figure 8: Total AMFs of O_3 (first row), NO_2 (second row), OClO (third row) and BrO (fourth row) computed for Marambio 2018, for surface albedo=0: Sunrise values at left and sunset values at right. Red symbols correspond to NDACC AMFs for O_3 and NO_2 [Hendrick et al, 2011], OClO AMFs from Pinardi et al., 2022 and BrO AMFs from Fig. 2 of Theys et al., 2007. 2D-DISORT AMFs for February (violet crosses) and September (black squares) are also shown.

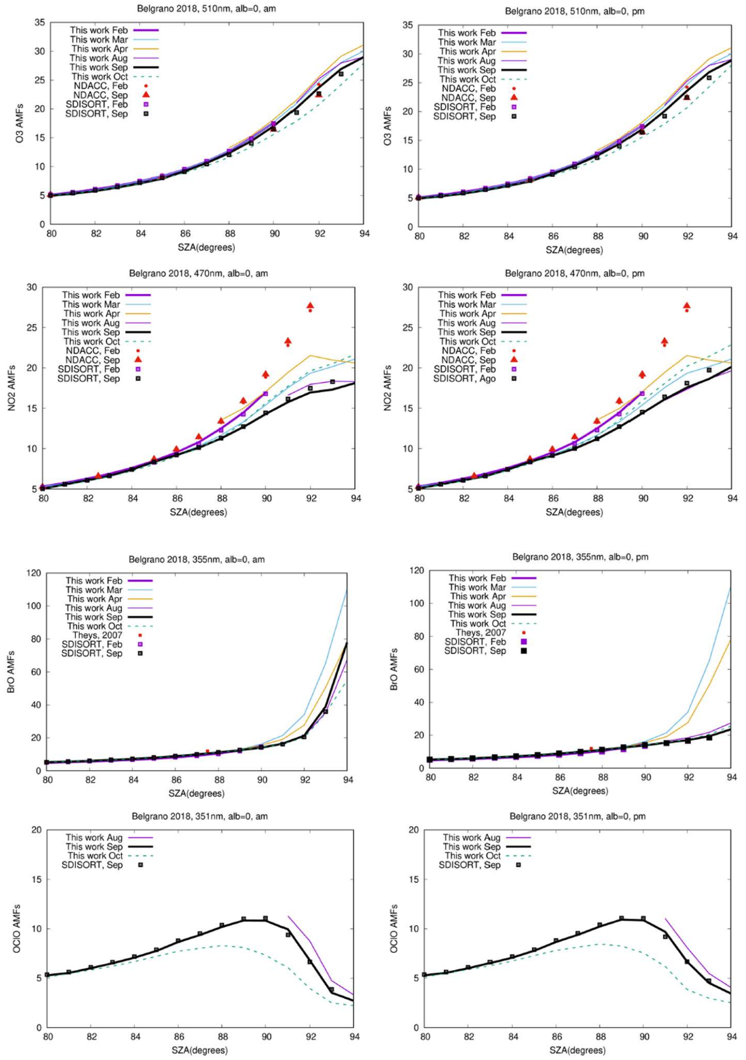
Belgrano 2018, 510nm, alb=0, am
Belgrano 2018, 510nm, alb=0, pm
Belgrano 2018, 470nm, alb=0, am
Belgrano 2018, 470nm, alb=0, pm
Belgrano 2018, 355nm, alb=0, am
Belgrano 2018, 355nm, alb=0, pm
Belgrano 2018, 351nm, alb=0, am
Belgrano 2018, 351nm, alb=0, pm

405 **Figure 9: Total AMFs of O$_3$ (first row), NO$_2$ (second row), OClO (third row) and BrO (fourth row) computed for Belgrano 2018, for surface albedo=0: Sunrise values at left and sunset values at right. Red symbols correspond to NDACC AMFs for O$_3$ and NO$_2$ [Hendrick et al, 2011] and BrO AMFs from Fig. 2 of Theys et al., 2007. 2D-DISORT AMFs for February (violet crosses) and September (black squares) are also shown.**

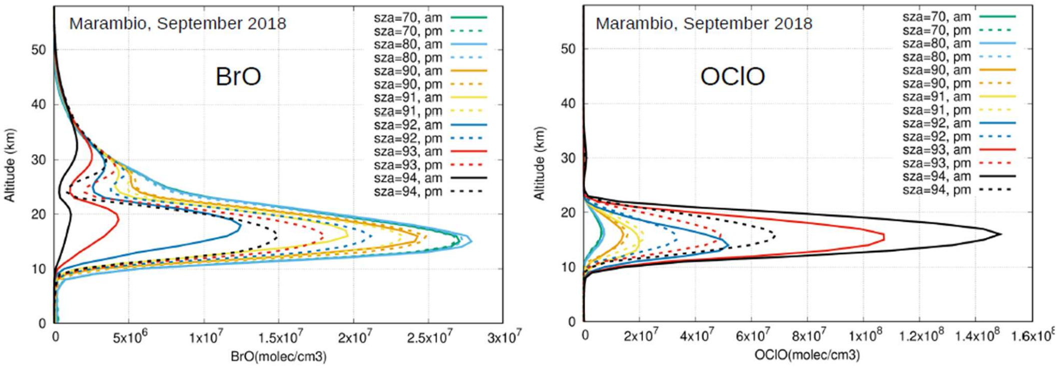

Figure 10: Evolution with SZA of the concentration of BrO (left) and OClO (right) over Marambio during September 2018. Concentration profiles have been obtained with the photochemical model based on SLIMCAT.

3.2 Comparison with measurements

To further verify the validity of our results, experimental SCDs obtained in 2018 using our ground-based DOAS instrument in Marambio have been compared with modelled SCDs (see Fig. 11). Note that for OClO, the detection limit is about 1.0×10^{14} molecules/cm^2, thus measurements below this detection limit have not been included in the figure. We have compared SCDs calculated and measured at SZA=90° since that SZA is a good compromise in terms of instrumental signal-to-noise ratio for twilight observations. Similar results (not shown) have been found for SZA=92°. For comparison, experimental and modelled SCDs have been averaged in a 10-day period and represented in the middle of the period considered. Error bars of experimental data represent the standard deviation of all the points used in the average. Modelled SCDs are obtained from the calculated Box-AMFs, considering photochemistry, Earth sphericity and the optical path averages described in previous sections. In practice, the analysis of measured spectra provides differential SCDs (dSCDs) against a given reference (see Section 3). This reference is usually selected for conditions at which the contribution of the SCD of the target trace gas is a minimum. When studying stratospheric SCDs, the reference is also chosen to minimise the possible contribution from tropospheric absorbers. For the case of interest in this work, these conditions are met at the beginning or at the end of the calendar year. In Figure 10, the modelled reference SCD have been added to the experimental dSCDs to estimate the experimental SCDs. To do so, the exact experimental conditions (fractional day, SZA) of the reference have been used in the reference content calculation, obtaining a value of 1.34×10^{19} molec/cm^2 for O_3, 5.76×10^{15} molec/cm^2 for NO_2, 6.51×10^{13} molec/cm^2 for BrO and 2.55×10^{11} molec/cm^2 for OClO.

All year round, measured O_3 SCDs are very well captured by mean and std modelled values (less than 7.7% difference), which give us confidence in the methodology used in this work. Regarding NO_2, measured and modelled SCDs agree within the one sigma std of the measurements accumulated in 10-day periods. Regarding BrO, modelled SCDs are smaller than observations, particularly for winter, with a maximum relative difference of ~20%. Similar differences can be seen for mean measured-modelled OClO, although in this case values fall within the once sigma variability of the measurements. Regarding BrO, frequent tropospheric bromine explosions have been reported at Marambio [Prados-Roman et al., 2025], which could lead to a contamination of the observed SCD by tropospheric BrO even at high SZA.

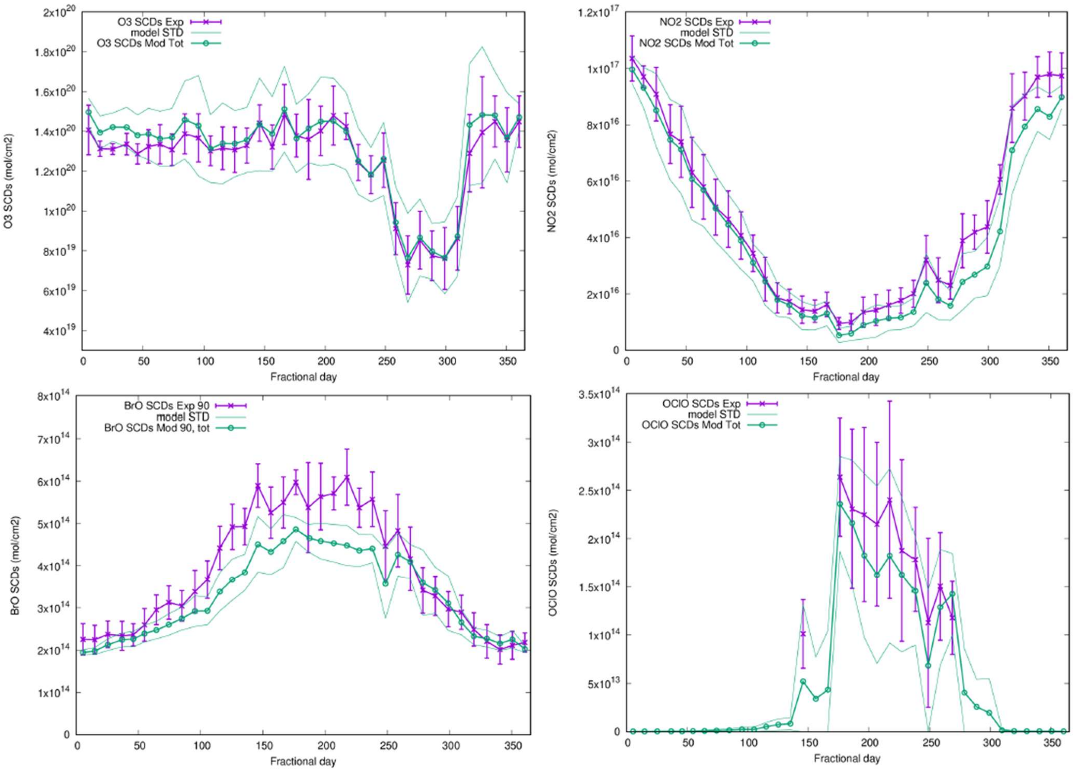

Figure 11: Measured (violet) and modelled (green) O_3 (top, left), NO_2 (top, right), BrO (bottom, left) and OClO (bottom, right) SCDs for Marambio 2018, and SZA=90º. Fine green lines in the figure represents the modelled SCDs considering the mean concentration plus/minus the standard deviation of the concentration of each considered 10-day period.

In Figure 12, the evolution of the measured SCDs with the SZA (violet for am and green for pm) and the corresponding modelled values (yellow for am and blue for pm) have been represented for Marambio in September. In addition, to consider the possible impact of tropospheric BrO emissions, SCDs simulated with an added tropospheric contribution representative of what is observed at Marambio at this time of the year (1.3×10^{13} molec/cm^3 in the lower 5 km of the atmosphere Marambio [Prados-Roman et al., 2025]), are also plotted. For both cases only the stratospheric contribution (yellow and blue) and with an additional tropospheric contribution (black and red) for surface albedo = 0 (dashed lines) and = 1 (solid lines) are shown. While the surface albedo has a small influence in the "pure" stratospheric SCDs, when considering an extra BrO tropospheric contribution, the role of the albedo becomes important. As can be seen, when considering this tropospheric BrO contribution, modelled BrO SCDs fall within the std of the measured SCDs. This strengthens support for the hypothesis of tropospheric BrO as being the main cause of the observed differences between measured and modelled BrO SCDs shown in Figure 11.

Additional possible sources of error for all modelled SCDs could be the estimation of the SCD in the reference spectrum. Moreover, we must consider the limited spatial resolution of the SLIMCAT 3-D chemical transport model simulation used (2.8° × 2.8º). During active vortex periods, this limited model resolution may complicate the comparison with observations, particularly in Marambio, which is highly affected by the dynamics of the polar volar edge. The further detailed analysis of the differences found herein is beyond the scope of this work and will be the subject of future studies.

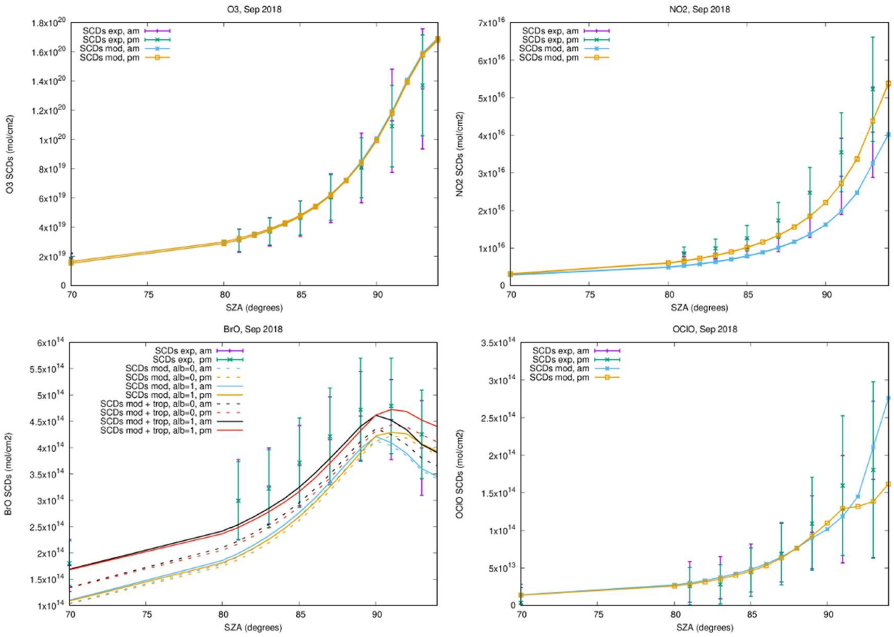

Figure 12: Solar zenith angle evolution of the monthly SCDs of O_3 (top left), NO_2 (top right), BrO (bottom left) and OClO (bottom right) over Marambio during September 2018. Violet and green lines are measured values (am and pm respectively). Blue and yellow lines are modelled values (am and pm respectively). To take into account possible tropospheric BrO explosions, simulated SCD values considering a tropospheric BrO contribution representative of the BrO values observed at Marambio during September (1.3×10^{13} mol/cm^3 in the first 5 km) have been included as black and red lines (am and pm respectively) in the BrO panel (bottom left).). In the BrO panel, solid lines correspond to surface albedo = 1, and dashed lines to surface albedo = 0.

5 Conclusions

Stratospheric AMFs for O_3, NO_2, BrO and OClO at Marambio and Belgrano Antarctic stations have been calculated for the year 2018. They have been obtained by using a spherical Monte-Carlo RTM. Temperature, pressure and optical path averaged concentration vertical profiles obtained from a photochemical box-model have been used as input in the RTM. These optical path averages have been calculated taking into account the different SZAs encountered by the sunlight beams during twilight. To our knowledge, BrO and OClO stratospheric AMFs are reported for the first time for SZAs up to 94º taking into account photochemistry and optical path averages of the concentrations.

In order to simplify the complex calculations, monthly averaged AMFs have been calculated (see values in Supplementary Material). The impact of the temporal sampling in the calculation of these quantities has been studied, concluding that for NO_2 and OClO shorter temporal sampling is recommended especially during the months of June and July.

Comparing the obtained O_3 and NO_2 AMFs with those provided by 2D-DISORT, a good agreement is found. However, when comparing with NDACC AMFs, while all sets of data show similar results for O_3, for NO_2 larger differences are observed. Considering that 2D-DISORT and MYSTIC simulations produce similar results, these differences are attributed to the different concentration profiles used as input in NDACC as compared to the photochemical concentration profiles used in this work.

Our results show that, for photo reactive species as the considered in this work, the evolution of the AMFs and SCDs with the SZA mainly relays on their photochemical variations (total concentration and its vertical distribution), the optical path followed by the sunlight beams, i.e. the geometry of the problem (observation view, Earth sphericity, Sun position, etc), and the effective scattering altitude.

To validate our results, simulated SCDs of the four considered compounds have been compared to measurements performed in Marambio. A general good agreement is found for O_3, NO_2 and OClO. Although some discrepancies are found at winter for BrO, they can be attributed (mostly) to the contribution of the tropospheric BrO that is not taken into account in the photochemical profiles, but that have a significant influence on the total BrO SCDs even for zenith measurements. In that case (of large tropospheric contribution) surface albedo significantly influences the results. In general, for all four species, a good agreement is found within one sigma standard deviation. This confirms the validity of the method employed and the approximations considered.

Author contributions

LGM: Conceptualization, data curation, formal analysis, investigation, methodology, software, project administration, supervision, validation, visualization and writing; CPR: Conceptualization, data curation, formal analysis, investigation, validation, writing and funding acquisition; MPC: data curation, formal analysis, investigation and validation; MvR: conceptualization, formal analysis, investigation, methodology, software, and validation; OP: resources, MNC: data curation, software; HO: resources; MY: conceptualization, data curation, formal analysis, funding acquisition, investigation, validation and resources.

Acknowledgements

The authors would like to acknowledge the work done by the technical teams at the stations of Belgrano and Marambio.

Financial support

This work was supported by the Spanish Ministry of Science, Innovation and Universities (Ministerio de Ciencia, Innovacion y Universidades) under grant PID2021-122737NB-I00 (project GARDENIA).

References

Adams C., Strong, K., Batchelor, R. L., Bernath, P. F, Brohede, S., Boone, C., Degenstein, D., Daffer, W. H., Drummond, J. R., Fogal, P. F., Farahani, E., Fayt, C., Fraser, A., Goutail, F., Hendrick, F., Kolonjari, F., Lindenmaier, R., Manney, G.,McElroy, C. T., McLinden, C. A., Mendonca, J., Park, J.-H., Pavlovic, B., Pazmino, A., Roth, C., Savastiouk, V., Walker, K. A., Weaver, D. and Zhao, X.: Validation of ACE and OSIRIS ozone and NO2 measurements using ground-based instruments at 80º N, Atmos. Meas. Tech., 5, 927–953, doi:10.5194/amt-5-927-2012, 2012.

Aliwell, S. R., Van Roozendael, M., Johnston, P.V., Richter, A., Wagner, T., Arlander, D.W., Burrows, J.P., Fish, D.J., Jones, R.L., Tørnkvist, K.K., Lambert, J.C., Pfeilsticker, K., Pundt, I.: Analysis for BrO in zenith-sky spectra: An intercomparison exercise for analysis improvement, J. Geophys. Res., 107, ACH 10-1 – ACH 10-20, 2002.

Barthia, P. K., C. G. Wellemeyer, S. L. Taylor, N. Nath, and A. Gopolan, Solar Backscatter (SBUV) Version 8 profile algorithm, Proceedings of the Quadrennial Ozone Symposium 2004, edited by C. Zerefos, pp. 295-296, Athens, Greece, ISBN, 960-630-103-6, 2004.

Chipperfield, M. P.: Multiannual simulations with a three-dimensional chemical transport model, J. Geophys. Res., 104(D1), 1781–1805, doi:10.1029/98JD02597, 1999.

Chipperfield, M. P.: New version of the TOMCAT/SLIMCAT offline chemical transport model: intercomparison of stratospheric tracer experiments, Q. J. Roy. Meteor. Soc., 132, 1179–1203, doi:10.1256/qj.05.51, 2006.

Chong, H., González Abad, G., Nowlan, C. R., Miller, C. C., Saiz-Lopez, A., Fernandez, R. P., Kwon, H.-A., Ayazpour, Z., Wang, H., Souri, A. H., Liu, X., Chance, K., O'Sullivan, E., Kim, J., Koo, J.-H., Simpson, W. R., Hendrick, F., Querel, R., Jaross, G., Seftor, C., and Suleiman, R. M.: Global retrieval of stratospheric and tropospheric BrO columns from OMPS-NM onboard the Suomi-NPP satellite, Atmos. Meas. Tech., 17, 2873–2916, https://doi.org/10.5194/amt-17-2873-2024, 2024.

Crutzen P. J.: The role of NO and NO2 in the chemistry of the troposphere and stratosphere, Ann. Rev. Earth Planet. Sci., 7, 443-72, 1979.

Denis, L., Roscoe, H. K., Chipperfield, M. P., Van Roozendael, M., and Goutail, F.: A new software suite for NO2 vertical profile retrieval from ground-based zenith-sky spectrometers, J. Quant. Spectrosc. Rad. Transf., 92, 321–333, doi:10.1016/j.jqsrt.2004.07.030, 2005.

Deutschmann, T.: On Modeling Elastic and Inelastic Polarized Radiation Transport in the Earth Atmosphere with Monte Carlo Methods, PhD thesis, University of Leipzig, Leipzig, Germany, 2014.

Deutschmann, T., Beirle, S., Frieß, U., Grzegorski, M., Kern, C., Kritten, L., Platt, U., Pukıte, J.,Wagner, T.,Werner, B., and Pfeilsticker, K.: The Monte Carlo Atmospheric Radiative Transfer Model McArtim: Introduction and Validation of Jacobians and 3D Features, J. Quant. Spectrosc. Ra., 112, 1119–1137, 2011.

Dhomse, S.S., M.P. Chipperfield, W. Feng, R. Hossaini, G.W. Mann, M.L. Santee, and M. Weber: A single-peak-structured solar cycle signal in stratospheric ozone based on Microwave Limb Sounder observations and model simulations, Atmos. Chem. Phys., 22, 903-916, doi:10.5194/acp-22-903-2022, 2022.

Emde, C., Buras, R., Mayer, B., Blumthaler, M.: The impact of aerosols on polarized sky radiance: model development, validation, and applications, Atmos. Chem. Phys., 10, 383–396, https://doi.org/10.5194/acp-10-383-2010, 2010.

Emde, C., Buras-Schnell, R., Kylling, A., Mayer, B., Gasteiger, J., Hamann, U., Kylling, J., Richter, B., Pause, C., Dowling, T., Bugliaro, L.: The libRadtran software package for radiative transfer calculations (version 2.0.1), Geosci. Model Dev., 9, 1647–1672, https://doi.org/10.5194/gmd-9-1647-2016, 2016.

Errera, Q. and Fonteyn, D.: Four-dimensional variational chemical assimilation of CRISTA stratospheric measurements, J. Geophys. Res.-Atmos., 106, 12253–12265, https://doi.org/10.1029/2001JD900010, 2001.

Fernandez, R. P., Carmona-Balea, A., Cuevas, C. A., Barrera, J. A., Kinnison, D. E., Lamarque, J.-F., Blaszczak-Boxe, C., Kim, K., Choi, W., Hay, T., Blechschmidt, A.-M., Schönhardt, A. Burrows, J. P., and Saiz-Lopez, A.: Modeling the sources and chemistry of polar tropospheric halogens (Cl, Br, and I) using the CAM-Chem global chemistry-climate model, J. Adv. Model. Earth Syst., 11, 2259–2289, https://doi.org/10.1029/2019MS001655, 2019.

Finkenzeller, H. and Volkamer, R.: O2–O2 CIA in the gas phase: Cross-section of weak bands, and continuum absorption between 297–500 nm, Journal of Quantitative Spectroscopy and Radiative Transfer, 279, 108 063, https://doi.org/10.1016/j.jqsrt.2021.108063, 2022.

Flynn, L., Long, C., Wu, X., Evans, R., Beck, C. T., Petropavlovskikh, I., McConville, G., Yu, W., Zhang, Z., Niu, J., Beach, E., Hao, Y., Pan, C., Sen, B., Novicki, M., Zhou, S., Seftor, C.: Performance of the Ozone Mapping and Profiler Suite(OMPS) products. Journal of Geophysical Research: Atmospheres, 119(10), 6181–6195. https://doi.org/10.1002/2013JD020467, 2014.

Gil, M., Puentedura, O., Yela, M., Parrondo, C., Jadhav, D. B., and Thorkelsson, B.: OClO, NO2 and O3 total column observations over Iceland during the winter 1993/94, Geophys. Res. Lett., 23, 3337–3340, https://doi.org/10.1029/96GL03102, 1996.

Gil, M., Yela, M., Gunn, L. N., Richter, A., Alonso, I., Chipperfield, M. P., Cuevas, E., Iglesias, J., Navarro, M., Puentedura, O., and Rodríguez, S.: NO2 climatology in the northern subtropical region: diurnal, seasonal and interannual variability, Atmos. Chem. Phys., 8, 1635–1648, https://doi.org/10.5194/acp-8-1635-2008, 2008.

Gomez-Martin, L., Toledo, D., Prados-Roman, C., Adame, J. A., Ochoa, H., and Yela, M.: Polar Stratospheric Clouds Detection at Belgrano II Antarctic Station with Visible Ground- Based Spectroscopic Measurements, Remote Sens., 13, 1412, https://doi.org/10.3390/rs13081412, 2021.

Hendrick, F., Barret, B., Van Roozendael, M., Boesch, H., Butz, A., De Mazière, M., Goutail, F., Hermans, C., Lambert, J.-C., Pfeilsticker, K., and Pommereau, J.-P.: Retrieval of nitrogen dioxide stratospheric profiles from ground-based zenithsky UV-visible observations: validation of the technique through correlative comparisons, Atmos. Chem. Phys., 4, 2091–2106, https://doi.org/10.5194/acp-4-2091-2004, 2004.

Hendrick, F., Van Roozendael, M., Kylling, A., Petritoli, A., Rozanov, A., Sanghavi, S., Schofield, R., von Friedeburg, C., Wagner, T., Wittrock, F., Fonteyn, D., and De Mazière, M.: Intercomparison exercise between different radiative transfer models used for the interpretation of ground-based zenith-sky and multi-axis DOAS observations, Atmos. Chem. Phys., 6, 93–108, https://doi.org/10.5194/acp-6-93-2006, 2006.

Hendrick, F., Van Roozendael, M., Chipperfield, M. P., Dorf, M., Goutail, F., Yang, X., Fayt, C., Hermans, C., Pfeilsticker, K., Pommereau, J.-P., Pyle, J. A., Theys, N., and De Mazière, M.: Retrieval of stratospheric and tropospheric BrO profiles and columns using ground-based zenith-sky DOAS observations at Harestua, 60ºN, Atmos. Chem. Phys., 7, 4869–4885, https://doi.org/10.5194/acp-7-4869-2007, 2007.

Hendrick, F., Pommereau, J.-P. , Goutail, F., Evans, R. D., Ionov, D., Pazmino, A., Kyrö, E., Held, G., Eriksen, P., Dorokhov, V., Gil, M. and Van Roozendael, M.: NDACC/SAOZ UV-visible total ozone measurements: improved retrieval and comparison with correlative ground-based and satellite observations, Atmos. Chem. Phys., 11, 5975–5995, doi:10.5194/acp-11-5975-2011, 2011.

Hersbach, H., Bell, B., Berrisford, P., Hirahara, S., Horányi, A., Muñoz-Sabater, J., Nicolas, J., Peubey, C., Radu, R., Schepers, D., Simmons, A., Soci, C., Abdalla, S., Abellan, X., Balsamo, G., Bechtold, P., Biavati, G., Bidlot, J., Bonavita, M., De Chiara, G., Dahlgren, P., Dee, D., Diamantakis, M., Dragani, R., Flemming, J., Forbes, R., Fuentes, M., Geer, A., Haimberger, L., Healy, S., Hogan, R. J., Hólm, E., Janisková, M., Keeley, S., Laloyaux, P., Lopez, P., Lupu, C., Radnoti, G., de Rosnay, P., Rozum, I., Vamborg, F., Villaume, S., Thépaut, J. N.: The ERA5 global reanalysis, Quarterly Journal of the Royal Meteorological Society, 146, 1999-2049, https://doi.org/10.1002/qj.3803, 2020.

Koenig, T. K., Hendrick, F., Kinnison, D., Lee, C. F., Van Roozendael, M. and Volkamer, R.: Troposphere–stratosphere-integrated bromine monoxide (BrO) profile retrieval over the central Pacific Ocean, Atmos. Meas. Tech., 17, 5911–5934, https://doi.org/10.5194/amt-17-5911-2024 , 2024.

Kreher, K., Van Roozendael, M., Hendrick, F., Apituley, A., Dimitropoulou, E., Frieß, U., Richter, A., Wagner, T., Lampel, J., Abuhassan, N., Ang, L., Anguas, M., Bais, A., Benavent, N., Bösch, T., Bognar, K., Borovski, A., Bruchkouski, I., Cede, A., Chan, K. L., Donner, S., Drosoglou, T., Fayt, C., Finkenzeller, H., Garcia-Nieto, D., Gielen, C., Gómez-Martín, L., Hao, N., Henzing, B., Herman, J. R., Hermans, C., Hoque, S., Irie, H., Jin, J., Johnston, P., Khayyam Butt, J., Khokhar, F., Koenig, T. K., Kuhn, J., Kumar, V., Liu, C., Ma, J., Merlaud, A., Mishra, A. K., Müller, M., Navarro-Comas, M., Ostendorf, M., Pazmino, A., Peters, E., Pinardi, G., Pinharanda, M., Piters, A., Platt, U., Postylyakov, O., Prados-Roman, C., Puentedura, O., Querel, R., Saiz-Lopez, A., Schönhardt, A., Schreier, S. F., Seyler, A., Sinha, V., Spinei, E., Strong, K., Tack, F., Tian, X., Tiefengraber, M., Tirpitz, J.-L., van Gent, J., Volkamer, R., Vrekoussis, M., Wang, S., Wang, Z., Wenig, M., Wittrock, F., Xie, P. H., Xu, J., Yela, M., Zhang, C., and Zhao, X.: Intercomparison of NO2, O4, O3 and HCHO slant column measurements by MAX-DOAS and zenith-sky UV–visible spectrometers during CINDI-2, Atmos. Meas. Tech., 13, 2169–2208, https://doi.org/10.5194/amt-13-2169-2020, 2020.

Kromminga, H., Orphal, J., Spietz, P., Voigt, S. and Burrows, J.P.: New measurements of OClO absorption cross-sections in the 325–435 nm region and their temperature dependence between 213 and 293 K, J. of Photochem. And Photobioloy A: Chemistry, 157, Issues 2–3, 149-160, https://doi.org/10.1016/S1010-6030(03)00071-6 , 2003.

Kühl, S., A. Do¨rnbrack, W. Wilms-Grabe, B.-M. Sinnhuber, U. Platt, and T. Wagner: Observational evidence of rapid chlorine activation by mountain waves above northern Scandinavia, J. Geophys. Res., 109, D22309, doi:10.1029/2004JD004797, 2004.

Kurucz, R.L.: Synthetic infrared spectra in Infrared Solar Physics, IAU Symp. 154, edited by D.M. Rabin and J.T. Jefferies, Kluwer, Acad., Norwell, MA, 1992.

Kylling, A. and Mayer, B.: LibRadTran: A package for UV and visible radiative transfer calculations in the Earth's atmosphere, http://www.libradtran.org, 2003.

Lamarque, J.-F., Emmons, L. K., Hess, P. G., Kinnison, D. E., Tilmes, S., Vitt, F., Heald, C. L., Holland, E. A., Lauritzen, P. H., Neu, J., Orlando, J. J., Rasch, P. J., and Tyndall, G. K.: CAM-chem: description and evaluation of interactive atmospheric chemistry in the Community Earth System Model, Geosci. Model Dev., 5, 369–411, https://doi.org/10.5194/gmd-5-369-2012, 2012.

Lambert, J.-C., J. Granville, M. Van Roozendael, A. Sarkissian, F. Goutail, J.-F. Müller, J.-P. Pommereau, and J.M. Russell III: A climatology of NO_2 profile for improved Air Mass Factors for ground-based vertical column measurements, in Stratospheric Ozone 1999, N.R.P. Harris, M. Guirlet, and G.T. Amanatidis (Eds.), Air Pollution Research Report 73 (CEC DG XII), pp. 703-706, 1999.

Lambert, J.-C., J. Granville, M. Van Roozendael, J.-F. Müller, F. Goutail, J.-P. Pommereau, A. Sarkissian, P. V. Johnston, and J. M. Russell III: Global Behaviour of Atmospheric NO_2 as Derived from the Integrated Use of Satellite, Ground-based Network and Balloon Observations, in Atmospheric Ozone - 19th Quad. Ozone Symp., Sapporo, Japan, 2000, Ed. by NASDA, pp. 201-202, 2000.

Lary, D. J.: Gas phase atmospheric bromine photochemistry, J. Geophys. Res., 101, 1505–1516, 1996.

Marquard, L. C., T. Wagner, and U. Platt: Improved air mass factorconcepts for scattered radiation differential optical absorption spectroscopy of atmospheric species, J. Geophys. Res., 105, 1315 – 1327, https://doi.org/10.1029/1999JD900340, 2000.

Mayer, B., Kylling, A.: Technical note: The libRadtran software package for radiative transfer calculations – descriptions and examples of use, Atmos. Chem. Phys., 5, 1855 – 1877, doi.org/10.5194/acp-5-1855-2005, 2005.

Mayer, B.: Radiative transfer in the cloudy atmosphere, in: EPJWeb of Conferences, EDP Sciences, Les Ulis, France, vol. 1, 75–99, https://doi.org/10.1140/epjconf/e2009-00912-1, 2009.

Mayer, B.: Radiative transfer code in the cloudy atmosphere, European Phys. J. Conferences, 1, 75–99, doi: 10.1140/epjconf/e2009-00912-1, 2009.

Mayer B., Hoch S.W., Whiteman C. D.: Validating the MYSTIC three-dimensional radiative transfer model with observations from the complex topography of Arizona's Meteor Crater, Atmos. Chem. Phys., 10, 8685–8696, doi:10.5194/acp-10-8685-2010, 2010.

McElroy, M. B., Salawitch, R. J., Wofsy, S. C., and Logan, J. A.: Reductions of Antarctic ozone due to synergistic interactions of chlorine and bromine, Nature, 321, 759–762, 1986.

Perliski, L.M. and Solomon, S.: On the Evaluation of Air Mass Factors for Atmospheric Near-Ultraviolet and Visible Absorption Spectroscopy, 98, 10363-10374, J. Geophys. Res., 1993.

Peters, E., Pinardi, G., Seyler, A., Richter, A., Wittrock, F., Bösch, T., Van Roozendael, M., Hendrick, F., Drosoglou, T., Bais, A. F., Kanaya, Y., Zhao, X., Strong, K., Lampel, J., Volkamer, R., Koenig, T., Ortega, I., Puentedura, O., Navarro-Comas, M., Gómez, L., Yela González,M., Piters, A., Remmers, J.,Wang, Y., Wagner, T., Wang, S., Saiz-Lopez, A., García-Nieto, D., Cuevas, C. A., Benavent, N., Querel, R., Johnston, P., Postylyakov, O., Borovski, A., Elokhov, A., Bruchkouski, I., Liu, H., Liu, C., Hong, Q., Rivera, C., Grutter, M., Stremme, W., Khokhar, M. F., Khayyam, J., and Burrows, J. P.: Investigating differences in DOAS retrieval codes using MAD-CAT campaign data, Atmos. Meas. Tech., 10, 955–978, https://doi.org/10.5194/amt-10-955-2017, 2017.

Pinardi, G., Van Roozendael, M., Hendrick, F., Richter, A., Valks, P., Alwarda, R., Bognar, K., Frieß, U., Granville, J., Gu, M., Johnston, P., Prados-Roman, C., Querel, R., Strong, K., Wagner, T., Wittrock, F. and Yela-Gonzalez, M.: Ground-based validation of the MetOp-A and MetOp-B GOME-2 OClO measurements, Atmos. Meas. Tech., 15, 3439–3463, https://doi.org/10.5194/amt-15-3439-2022, https://doi.org/10.1016/j.atmosenv.2025.121588, 2022.

Platt, U. and Stutz, J.: Differential Optical Absorption Spectroscopy (DOAS), Principle and Applications, ISBN: 3-340-21193-4, Springer Verlag, Heidelberg, 2008.

Prados-Roman, C., Gómez-Martín, L., Puentedura, O., Navarro-Comas, M., Iglesias, J., de Mingo, J.R., Pérez, M., Ochoa, H., Barlasina, M.E., Carbajal, G., Yela, M., 2018. Reactive bromine in the low troposphere of Antarctica: estimations at two research sites. Atmos. Chem. Phys. 18, 8549–8570. https://doi.org/10.5194/acp-18-8549- 2018.

Prados-Roman, C., Gomez-Martin, L., Adame, J. A., Puentedura, O., Navarro-Comas, M., Ochoa, H., and Yela, M. Tropospheric BrO in Western Antarctica: Distribution, Seasonality and Link to Sea Ice State of Development. Atmospheric Environment, 363, 121588, 2025.

Pukite, J., Borger, C., Döner, S., Gu, M. and Wagner T., OClO as observed by TROPOMI: a comparison with meteorological parameters and polar stratospheric cloud observations, Atmos. Chem. Phys., 22, 245–272, https://doi.org/10.5194/acp-22-245-2022, 2022.

Sander, S. P., and Friedl, R. R.: Kinetics and Product Studies of the Reaction ClO + BrO Using Flash Photolysis-Ultraviolet Absorption, J. Phys. Chem., 93, 4764–4771, 1989.

Schwaerzel M., Emde C., Brunner D., Morales R., Wagner T., Berne A., Buchmann B., Kuhlmann G.: Three-dimensional radiative transfer effects on airborne and ground-based trace gas remote sensing, Atmos. Meas. Tech., 13, 4277–4293, https://doi.org/10.5194/amt-13-4277-2020, 2020.

Serdyuchenko, A., Gorshelev, V., Weber, M., Chehade, W., and Burrows, J. P.: High spectral resolution ozone absorption crosssections– Part 2: Temperature dependence, Atmos. Meas. Tech., 7, 625–636, https://doi.org/10.5194/amt-7-625-2014, 2014.

Sinnhuber, B.-M., Sheode, N., Sinnhuber, M., Chipperfield, M. P., and Feng, W.: The contribution of anthropogenic bromine emissions to past stratospheric ozone trends: a modelling study, Atmos. Chem. Phys., 9, 2863–2871, 2009.

Solomon, S., Schmeltekopf, A. and Sanders R. W.: On the Interpretation of the Zenith Sky Absorption Measurements, J. Geophys. Res., 92, 8311-8319, https://doi.org/10.1029/JD092iD07p08311, 1987.

Solomon, S., Sanders, R. W., Miller, H. L.: Visible and Near Ultraviolet Spectroscopy at McMurdo Station, Antarctica 7. OClO Photochemistry and Ozone destruction, J. Geophys. Res., 95, 13807–13817, 1990.

Solomon, S., Haskins, J., Ivy, D. J., Min, F.: Fundamental differences between Arctic and Antarctic ozone depletion, PNAS, 111, 6220–6225, www.pnas.org/cgi/doi/10.1073/pnas.1319307111, 2014.

Spurr, R.: VLIDORT: A linearized pseudo-spherical vector discrete ordinate radiative transfer code for forward model and retrieval studies in multilayer multiple scattering media, J. Quant. Spectrosc. Radiat. Transf., 102, 316–342, 2006.

Spurr, R.: LIDORT and VLIDORT: Linearized pseudo-spherical scalar and vector discrete ordinate radiative transfer models for use in remote sensing retrieval problems, Springer Berlin, Heidelberg, https://doi.org/10.1007/978-3-540-48546-9_7, 2008.

Spurr, R. and Christi, M.: The LIDORT and VLIDORT linearized scalar and vector discrete ordinate radiative transfer models: Updates in the last 10 years, Springer, Cham, https://doi.org/10.1007/978-3-030-03445-0_1, 2019.

Theys, N., Van Roozendael, M., Hendrick, F., Fayt, C., Hermans, C., Baray, J.-L. , Goutail, F., Pommereau, J.-P. and De Mazière, M.: Retrieval of stratospheric and tropospheric BrO columns from multi-axis DOAS measurements at Reunion Island (21 S, 56 E), Atmos. Chem. Phys., 7, 4733–4749, https://doi.org/10.5194/acp-7-4733-2007, 2007.

WMO/UNEP Scientific Assessment of the Ozone Layer Depletion: 2022, https://www.unep.org/resources/publication/scientific-assessment-ozone-layer-depletion-2022, 2022.

WMO Ozone and UV Bulletin No. 3 – September 2025, https://library.wmo.int/idurl/4/69628, 2025.

Yela, M., Gil-Ojeda, M., Navarro-Comas, M., Gonzalez-Bartolomé, D., Puentedura, O., Funke, B., Iglesias, J., Rodríguez, S., García, O., Ochoa, H., Deferrari, G.: Hemispheric asymmetry in stratospheric NO2 trends, Atmos. Chem. Phys., 17, 13373–13389, https://doi.org/10.5194/acp-17-13373-2017, 2017.

Yela, M., Parrondo, C., Gil, M., Rodríguez, S., Araujo, J., Ochoa, H., Deferrari, G., and Díaz, S.: The September 2002 Antarctic vortex major warming as observed by visible spectroscopy and ozone soundings, Int. J. Remote Sens., 26, 3361–3376, https://doi.org/10.1080/01431160500076285, 2005.

Yung, Y. L., Pinto, J. P., Watson, R. T., and Sander, S. P.: Atmospheric bromine and ozone perturbations in the lower stratosphere, J. Atmos. Sci., 37, 339–353, 1980.

Zawada D., Franssens G., Loughman R., Mikkonen A., Rozanov A., Emde C., Bourassa A., Dueck S., Lindqvist H., Ramon D., Rozanov V., Dekemper E., Kyrölä E., Burrows J. P., Fussen D., Degenstein D.: Systematic comparison of vectorial spherical radiative transfer models in limb scattering geometry, Atmos. Meas. Tech., 14, 3953–3972, https://doi.org/10.5194/amt-14-3953-2021, 2021.